

## Self-organization of active colloids mediated by chemical interactions Supplementary information

Zhiwei Peng and Raymond Kapral\*  
*Chemical Physics Theory Group, Department of Chemistry,  
University of Toronto, Toronto, ON, M5S 3H6, Canada*  
(Dated: January 9, 2024)

### I. BINARY MIXTURE WITH SEQUENTIAL REACTION

#### A. Effect of the screening length

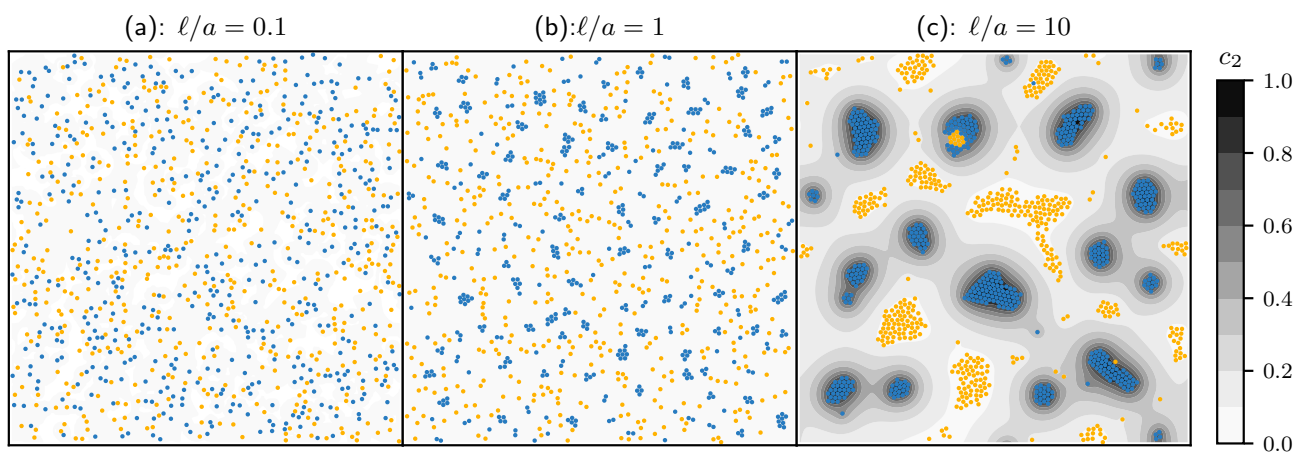


FIG. 1: Representative snapshots of the binary mixture undergoing the sequential reaction for different screening lengths. (a):  $\ell/a = 0.1$ , (b):  $\ell/a = 1$ , and (c):  $\ell/a = 10$ . Note that  $\Lambda_1 = a/\ell$ . For all simulations, the particles are initialized with random positions and orientations, the initial concentrations are  $c_1 = c_0$ ,  $c_2 = c_3 = 0$ . The system parameters are  $\phi = 0.1$ ,  $\hat{\mu}_{11} = -20$ ,  $\hat{\mu}_{22} = 20$ ,  $\Lambda_2 = 0.25$ ,  $Da_1 = Da_2 = 1/(2\pi) \approx 0.16$ ,  $\hat{\mu}_{12} = \hat{\mu}_{21} = 0$ ,  $\hat{\gamma}_{12} = \hat{\gamma}_{21} = 0$ , and  $\hat{\alpha}_1 = \hat{\alpha}_2 = \hat{\gamma}_{11} = \hat{\gamma}_{22} = 0$ .

For the sequential reaction scheme discussed in Sec. 4 of the main text, the chemical system is screened. The screening length plays an important role in controlling the dynamics and the resulting clustering of the binary mixture. Noting that the inverse screening length for the chemical species  $S_2$  is  $\lambda_1 = \sqrt{k_{b,1}/D}$ , we define the screening length as  $\ell = 1/\lambda_1$ .

In Fig. 1, we present snapshots of the binary mixture as a function of the dimensionless screening length  $\ell/a$ , where  $a$  is the radius of the particles. If  $\ell/a \ll 1$ , as shown in Fig. 1(a), the chemical concentration gradient is highly localized at the particle centers; as a result, other particles cannot respond to this gradient and no clusters will form. In Fig. 1(b),  $\ell/a = 1$ , particles can barely sense the presence of chemical gradients produced by other particles, and we observe the formation of small molecules. For large screening length, such as  $\ell/a = 10$  shown in Fig. 1(c), prominent cluster formation is observed. Because the gold particles are repelled from the blue ones (or regions of high concentration of  $S_2$ ), they aggregate in the regions with low concentration. This aggregation is a result of repulsive interactions with the surrounding blue clusters, and these ‘clusters’ of gold particles are loosely packed. This is different from the tight packing in the blue clusters, which are formed as a result of attractive interactions.

In Fig. 2, we plot the size of the largest cluster in the system, which is defined as the number of particles in the largest cluster, as a function of time. The sudden jumps in the maximum cluster size signify the merging of smaller clusters.

\* r.kapral@utoronto.ca

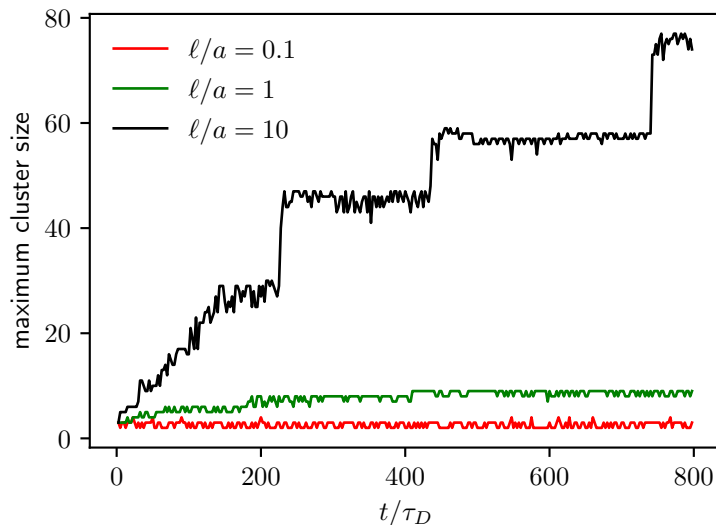


FIG. 2: Maximum cluster size as a function of time for different screening lengths. All simulation parameters are listed in the caption of Fig. 1.

### B. Variation of the relative magnitude of the phoretic coefficients

We consider the case in which  $\hat{\mu}_{11} < 0$  and  $\hat{\mu}_{22} > 0$ . We vary  $\hat{\mu}_{22}$  while keeping other parameters fixed. As shown in Fig. 3, the clustering dynamics varies significantly as a function of  $\hat{\mu}_{22}/\hat{\mu}_{11}$ . When  $\hat{\mu}_{22}$  is small (Fig. 3(a)), the attraction is weak so that the gold particles are not attached to the periphery of the blue clusters. In Fig. 3(b),  $\hat{\mu}_{22} = 20$ , the attraction allows the gold particles to attach to the blue clusters. If the attraction is too strong, the blue clusters can be destroyed by the gold particles, as shown in Fig. 3(c).

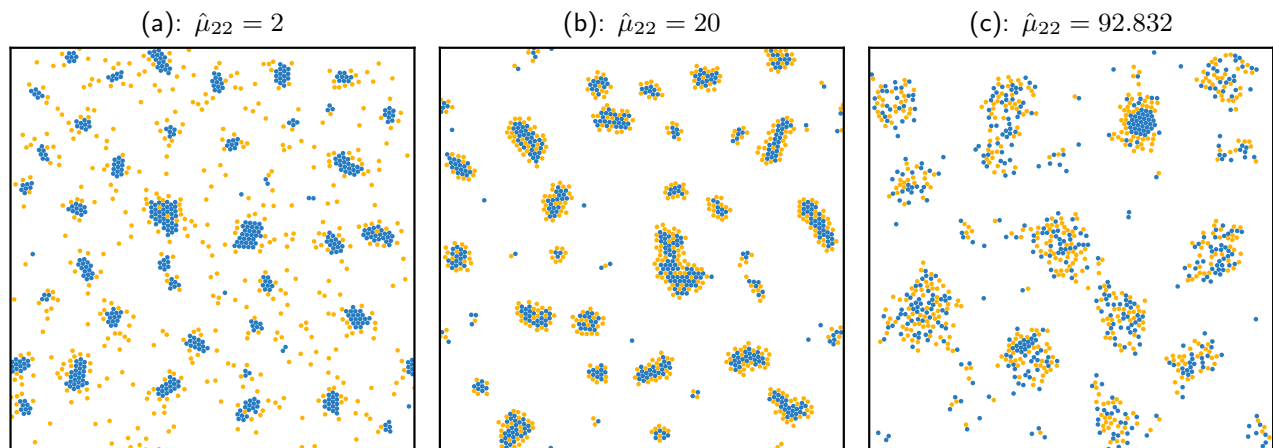


FIG. 3: Simulation snapshots of the binary mixture at  $t/\tau_D = 499$  for different values of  $\hat{\mu}_{22}$ . For all simulations, the particles are initialized with random positions and orientations, the initial concentrations are  $c_1 = c_0$ ,  $c_2 = c_3 = 0$ .

The system parameters are  $\phi = 0.1$ ,  $\hat{\mu}_{11} = -20$ ,  $\Lambda_1 = \Lambda_2 = 0.25$ ,  $Da_1 = Da_2 = 1/(2\pi) \approx 0.16$ ,  $\hat{\mu}_{12} = \hat{\mu}_{21} = 0$ ,  $\hat{\gamma}_{12} = \hat{\gamma}_{21} = 0$ , and  $\hat{\alpha}_1 = \hat{\alpha}_2 = \hat{\gamma}_{11} = \hat{\gamma}_{22} = 0$ .

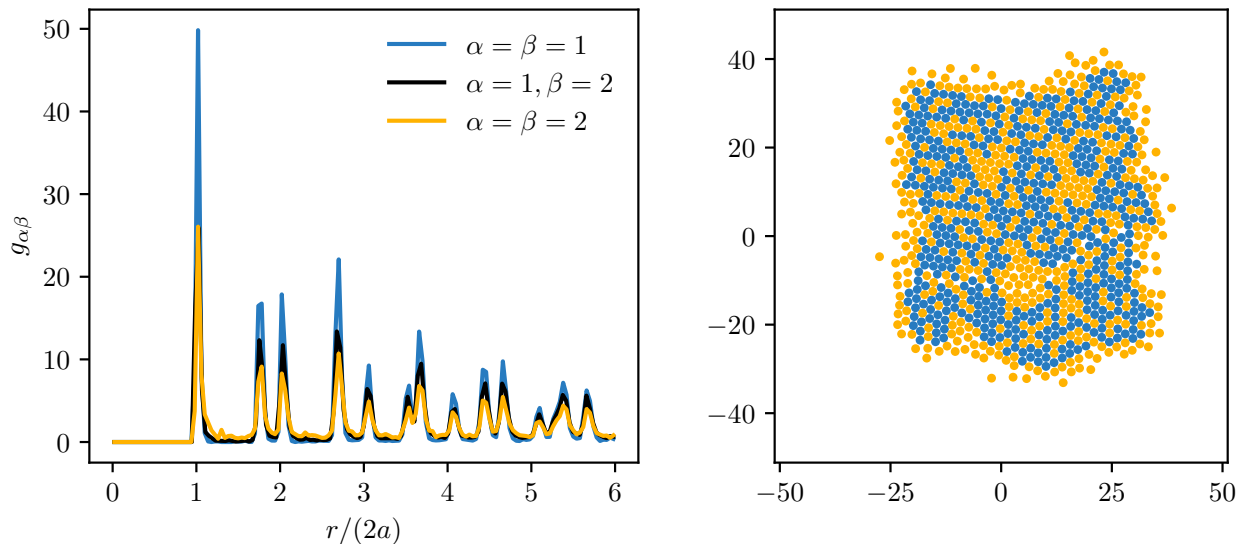


FIG. 4: Left: The self and cross RDFs of the binary mixture at  $\phi = 0.3$ . Right: The corresponding simulation snapshot of the binary mixture. The nonzero phoretic coefficients are  $\hat{\mu}_{11} = -20$ , and  $\hat{\mu}_{22} = 20$ . The particles are initialized with random positions and orientations, the initial concentrations are  $c_1 = c_0$ ,  $c_2 = c_3 = 0$ ,  $\Lambda_1 = \Lambda_2 = 0.25$ ,  $Da_1 = Da_2 = 1/(2\pi) \approx 0.16$ ,  $\hat{\mu}_{12} = \hat{\mu}_{21} = 0$ ,  $\hat{\gamma}_{12} = \hat{\gamma}_{21} = 0$ , and the number of type 1 particles are the same as 2,  $\hat{\alpha}_1 = \hat{\alpha}_2 = \hat{\gamma}_{11} = \hat{\gamma}_{22} = 0$ .

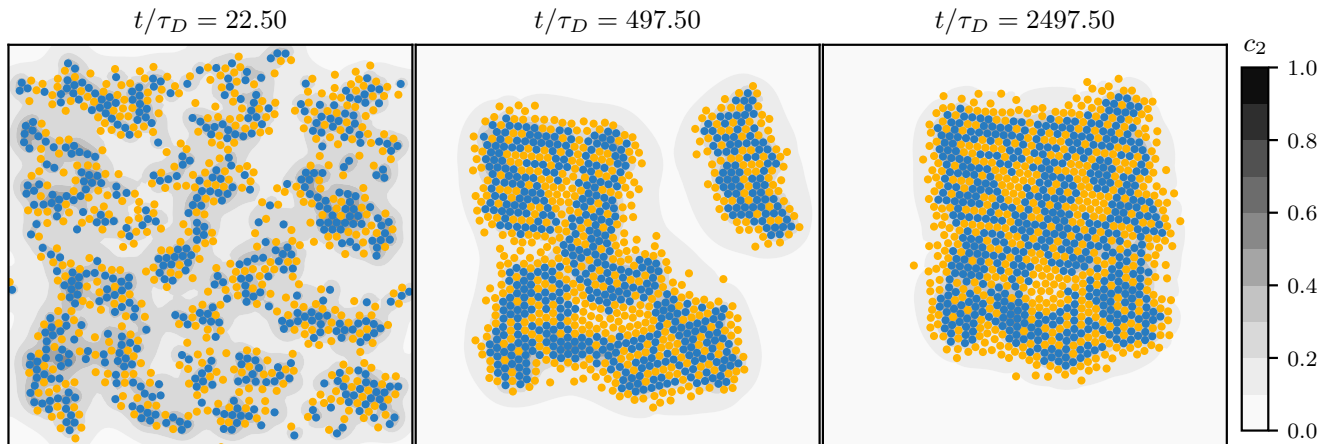


FIG. 5: Simulation snapshots of the binary mixture at different times. All simulation parameters are the same as those in Fig. 4.

### C. Higher particle densities

In Fig. 4, we plot the radial distribution functions (RDFs)  $g_{\alpha\beta}$  (left) and the corresponding system snapshot (right) at  $\phi = 0.3$ . In the RDFs, the subscripts denote the type of colloid with  $g_{11}$  being the self RDF of type 1 colloid,  $g_{22}$  being the self RDF of type 2 colloid, and  $g_{12}$  being the cross RDF of types 1 and 2. Because  $\mu_{11} < 0$  and  $\mu_{22} > 0$ , the binary mixture forms a heterogeneous cluster consisting of both types of colloids. In contrast to systems at low density ( $\phi = 0.1$ ) shown in the main text, the entire system collapses into a single cluster at  $\phi = 0.3$ . We observe that  $g_{11}$  has the largest peaks, followed by  $g_{12}$  and then  $g_{22}$ . This is consistent with the clustering process in which type 1 (blue) particles first aggregate and then type 2 (gold) particles are attracted towards the blue clusters. Apart from the magnitude of the peaks, the self and cross RDFs have a similar structure.

In Fig. 5, we show the simulation snapshots at different times. At short times, small clusters start to form. At intermediate times, cluster-cluster attraction leads to the merging of multiple clusters. At long times, the entire

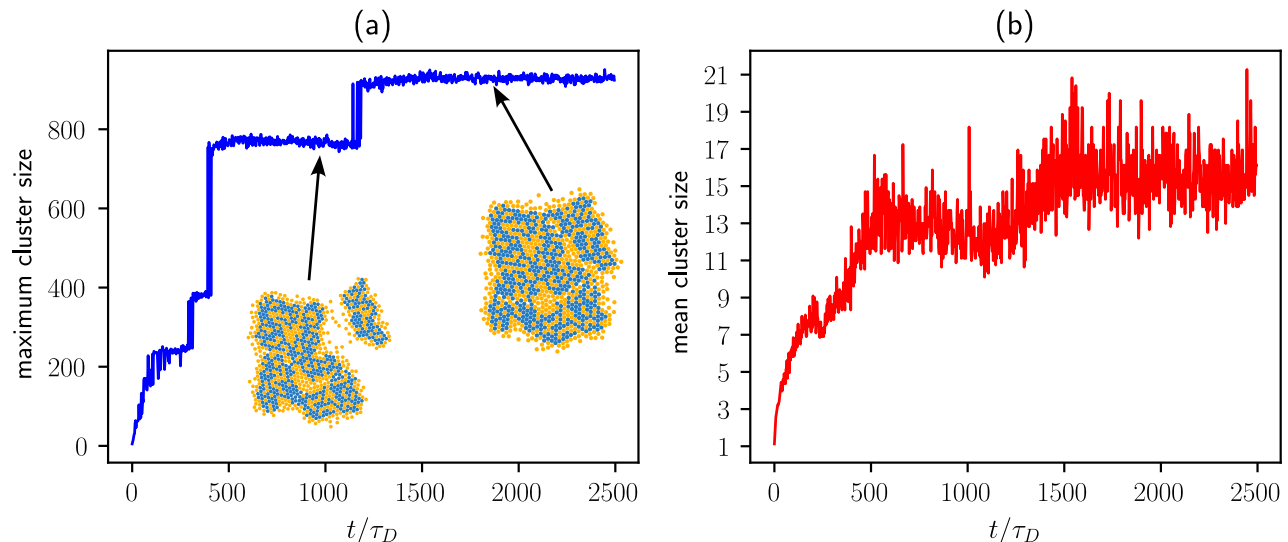


FIG. 6: (a) The maximum cluster size in the system as a function of time. The jumps in the maximum cluster size signify the merging of clusters. (b) The mean cluster size in the system as a function of time. Notice that the mean cluster size is significantly smaller than the maximum because an isolated particle is considered as a 1-particle cluster. All simulation parameters are the same as those in Fig. 4.

system collapses into a single cluster.

To illustrate the merging dynamics, we present the cluster size distributions as a function of time in Fig. 6. In Fig. 6(a), the size of the largest cluster in the system is plotted as a function of time. The sudden jumps in the maximum cluster size signifies the merging of smaller clusters as illustrated in the insets. In Fig. 6(b), the mean cluster size as a function of time is presented. Because gold particles on the periphery are loosely attached (not at contact) to the cluster, they are treated as 1-particle clusters and the resulting mean cluster size is significantly smaller than the maximum. The fluctuations in the cluster size curves represents fluctuations, which results from the random attachment and detachment of particles from the clusters.

In Fig. 7, we plot the radial distribution functions (RDFs)  $g_{\alpha\beta}$  (left) and the corresponding system snapshot (right) at  $\phi = 0.3$ . All parameters are the same as those in Fig. 4 except that the sign of  $\hat{\mu}_{22}$  is reversed. As a result, type 2 (gold) particles are repelled from type 1 (blue). Because type 2 particles are not clustering,  $g_{22}$  is largely flat as a function of the radial distance.

Due to the strong attraction between blue clusters, gold particles can be trapped as multiple smaller clusters aggregate into a single cluster. The gold particles in the bottom-left cluster in Fig. 7 shows such a trapped state. To illustrate the trapping dynamics, in Fig. 8 we plot the simulation snapshots at different times. At short times, small clusters of blue particles start to form and gold particles are pushed away from blue particles. At intermediate times, larger blue clusters are established and cluster-cluster attraction leads to the merging of multiple clusters. At long times, some gold particles are trapped inside a merged blue cluster.

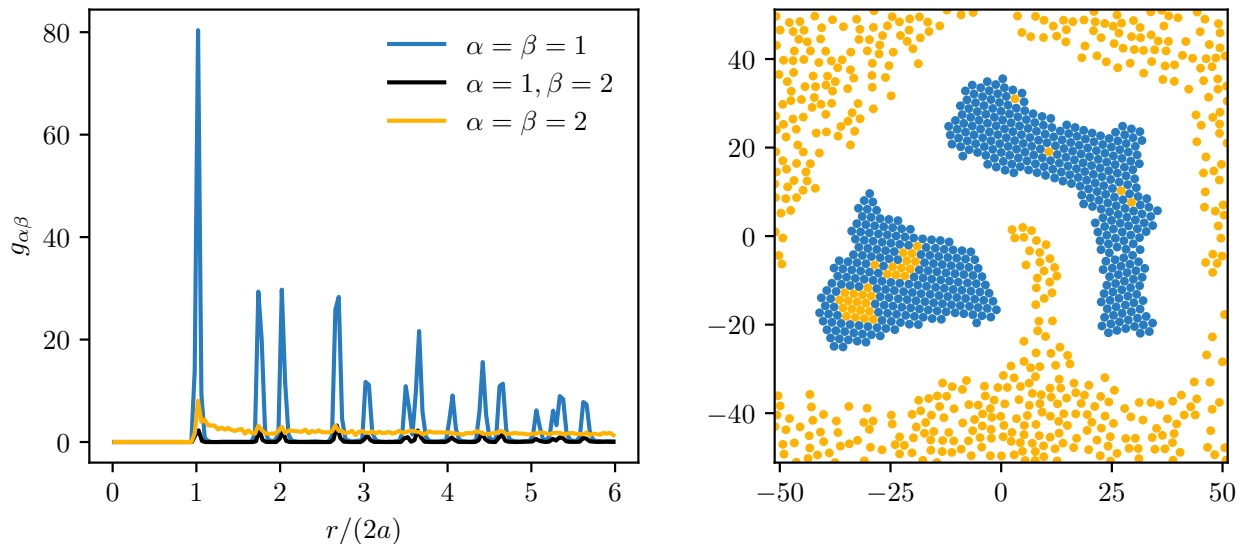


FIG. 7: Left: The self and cross RDFs of the binary mixture at  $\phi = 0.3$ . Right: The corresponding simulation snapshot of the binary mixture. The nonzero phoretic coefficients are  $\hat{\mu}_{11} = -20, \hat{\mu}_{22} = -20$ . The particles are initialized with random positions and orientations, the initial concentrations are  $c_1 = c_0, c_2 = c_3 = 0$ ,  $\Lambda_1 = \Lambda_2 = 0.25, Da_1 = Da_2 = 1/(2\pi) \approx 0.16, \hat{\mu}_{12} = \hat{\mu}_{21} = 0, \hat{\gamma}_{12} = \hat{\gamma}_{21} = 0$ , and the number of type 1 particles are the same as 2,  $\hat{\alpha}_1 = \hat{\alpha}_2 = \hat{\gamma}_{11} = \hat{\gamma}_{22} = 0$ .

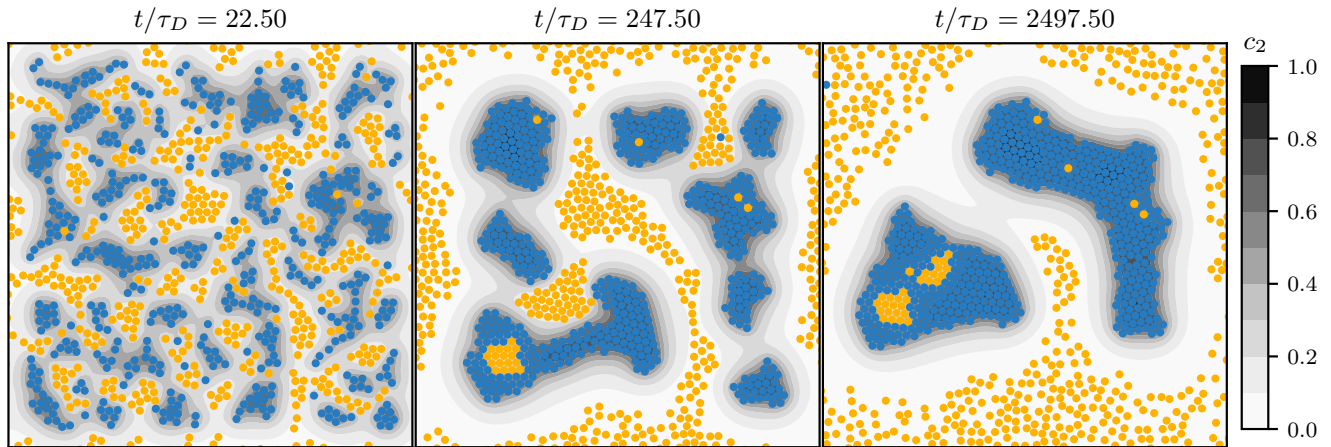


FIG. 8: Simulation snapshots of the binary mixture at different times. All simulation parameters are the same as those in Fig. 7.

## II. AUTOCATALYTIC REACTIONS

In this section, we consider the reversible Selkov model with a single colloidal type. In contrast to the binary mixture considered in the main text, here we do not have type 2 particles. On all particles we have  $S_1 + 2S_2 \xrightleftharpoons[k_2^-]{k_2^+} 3S_2$ . In the bulk fluid, we have  $F \xrightleftharpoons[k_1^-]{k_1^+} S_1$  and  $S_2 \xrightleftharpoons[k_3^-]{k_3^+} G$ , where  $F$  and  $G$  are held fixed by reservoirs and their concentrations do not enter the reaction kinetics directly.

The concentration of  $S_1$ , denoted by  $c_1$ , is governed by

$$\frac{\partial c_1}{\partial t} = D\nabla^2 c_1 + k_1^+ - k_1^- c_1 - \sum_{i=1}^N (k_2^+ c_1 c_2^2 - k_2^- c_2^3) \delta(\mathbf{x} - \mathbf{X}_i). \quad (1)$$

The concentration of  $S_2$ , or  $c_2$ , satisfies the equation

$$\frac{\partial c_2}{\partial t} = D\nabla^2 c_2 + k_3^- - k_3^+ c_2 + \sum_{i=1}^N (k_2^+ c_1 c_2^2 - k_2^- c_2^3) \delta(\mathbf{x} - \mathbf{X}_i). \quad (2)$$

In Fig. 9-11, the simulation parameters are as follows:  $\mu_1 = 10, \mu_2 = -10, \gamma_1 = \gamma_2 = 0, \Lambda_1 = 0.2, \Lambda_2 = 0.2, a = 1, D = 1, D_T = 0.1, k_1^+ = k_1^- = 0.04, k_3^+ = k_3^- = 0.04, k_2^+ = 0.1, k_2^- = 1, \phi = 0.1, N = 1000$ . In Fig. 6, we plot the maximum cluster size as a function of time. In Fig. 10, we plot the RDF at different times. In Fig. 11, we plot the system snapshots at different times.

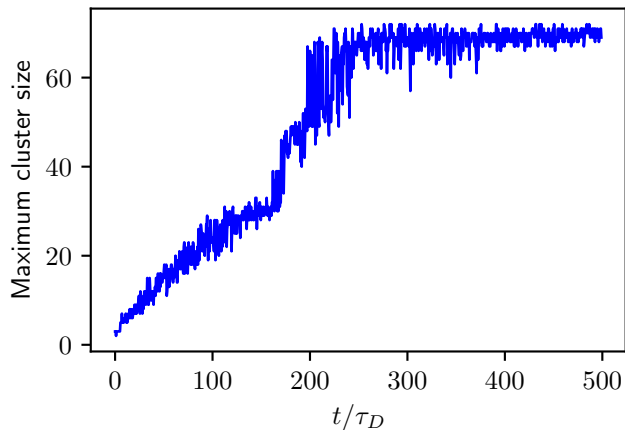


FIG. 9: The maximum cluster size in the system as a function of time.

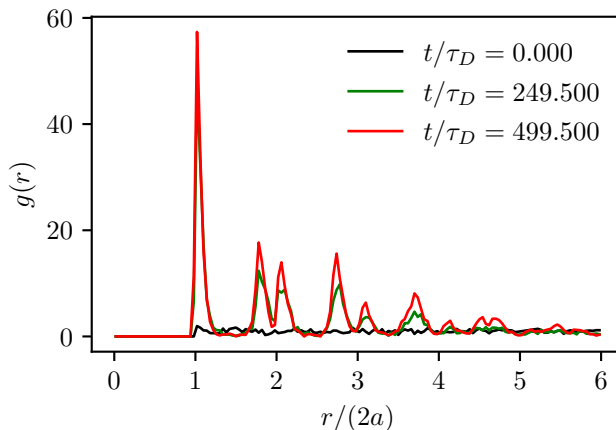


FIG. 10: The RDF as a function of  $r/(2a)$  at different times.

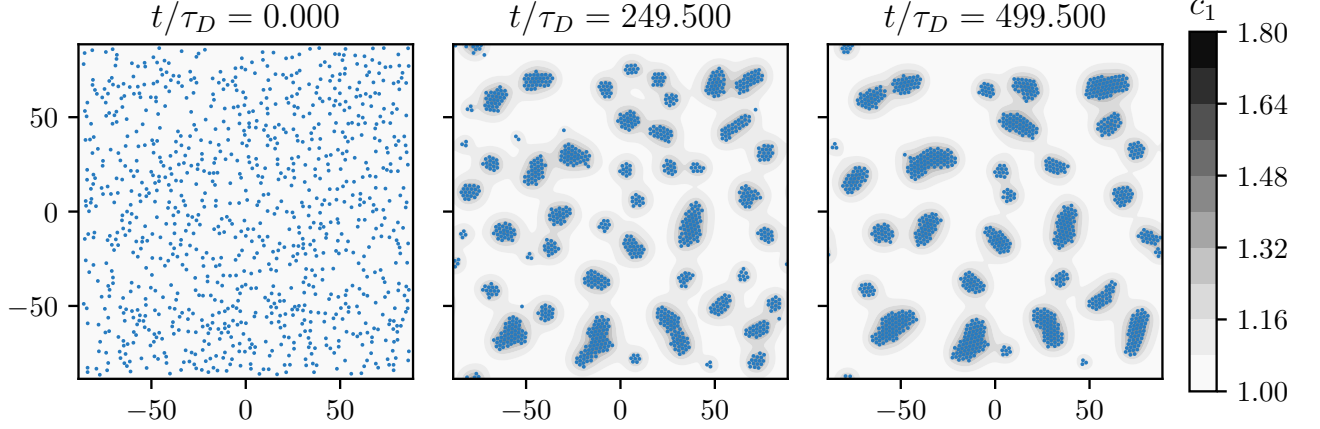


FIG. 11: Simulation snapshots of the system at different times. The contour plot shows the concentration field of  $S_1$ .

### III. CONTRIBUTIONS TO THE COLLOID REACTION RATE

Here we describe in more detail the contributions to the colloid reaction rate and the approximations that result in the expression for the reaction rate  $\sum_{K=1}^{n_r} \sum_{i_K=1}^{N_K} \mathcal{R}_{j,K}^s(\mathbf{c}^K) \delta(\mathbf{x} - \mathbf{X}_{i_K})$  in Eq. (1) of the main text. For simplicity we consider the single reversible reaction  $S_1 \rightleftharpoons S_2$  on the colloids with forward and reverse rate coefficients  $\kappa_{\pm}$ , where

$$\sum_{i=1}^N \mathcal{R}^s(\mathbf{c}) \delta(\mathbf{x} - \mathbf{X}_i) = - \sum_{i=1}^N (\kappa_+ c_1 - \kappa_- c_2) \delta(\mathbf{x} - \mathbf{X}_i). \quad (3)$$

A suspension of active Janus colloids with this surface reaction kinetics was analysed using a local nonequilibrium thermodynamics formulation that is consistent with microscopic reversibility and Onsager's reciprocal relations [1]. Denoting the reaction rate for species  $S_k$ ,  $k = 1, 2$  as  $w_k = -\nu_k w$ , where  $\nu_k$  is the stoichiometric coefficient,  $w$  can be expressed as a sum of products of Onsager coefficients and thermodynamic forces. A full presentation of this derivation is given in Ref. [1], along with a discussion of the the various contributions to  $w$  and their magnitudes. Here we outline these results using the notation of the present paper in order to assess the approximations to the local reaction rate that were made in our simulations. We refer to equations in Ref. [1] by a prefix ‘‘R’’.

Equation (R 57) gives the contributing Onsager coefficients and thermodynamic forces to the reaction rate as,

$$w \approx \beta L_{rr} A_{\text{rxn}} - \beta \mathbf{L}_{r1} \cdot \nabla \mu_1 - \beta \mathbf{L}_{r2} \cdot \nabla \mu_2 - \beta \mathbf{L}_{rC} \cdot \nabla \mu_C, \quad (4)$$

where  $A_{\text{rxn}} = \mu_1 - \mu_2$  is the chemical affinity and  $\mu_1$ ,  $\mu_2$  and  $\mu_C$  are the chemical potentials of the species  $S_1$ ,  $S_2$  and the colloids, respectively. Writing this expression in more detail we have (see (R B.14))

$$w \approx \sum_{i=1}^N \left( (\kappa_+ c_1 - \kappa_- c_2) + \tilde{\omega} \mathbf{u}_i \cdot (\kappa_+ \nabla c_1 - \kappa_- \nabla c_2) - \chi D_{\text{rxn}} \mathbf{u}_i \cdot (\nabla - \beta \mathbf{F}_i^P) \right) \delta(\mathbf{x} - \mathbf{X}_i). \quad (5)$$

The first term in this expression is just Eq. (3). In the second term that involves the species gradients, the parameter  $\tilde{\omega} \sim \mathcal{O}(a)$  and its lowest order approximation is  $\tilde{\omega} = 3a/4$ . Consequently this contribution should be smaller than the first term since  $a |\nabla c_k| < c_k$  and it depends on  $\mathbf{u}_i \cdot \nabla c_k$ , which will also reduce the importance of this contribution since neither the colloid orientation nor the gradient is controlled. The last term accounts for colloid gradients and its prefactor involves the diffusiophoretic coefficient  $\chi = V_{sd}/(\kappa_+ c_1 - \kappa_- c_2)$  and the reaction diffusivity  $D_{\text{rxn}} = (\kappa_+ c_1 + \kappa_- c_2)/2$ . Note that if an external force  $\mathbf{F}_{\text{ext}}$  is present there is an additional mechanical affinity,  $\beta \mathbf{F}_{\text{ext}}$ , and this force should be included in the last term. Since no external force is present in our calculations, we will not consider this term further. Its presence and effect on the global reaction rate of the colloidal suspension is discussed in Ref. [1].

For simplicity, we now consider the irreversible version of this reaction, in which case  $\kappa_+ = \kappa$ ,  $\kappa_- = 0$ ,  $\chi = \alpha/\kappa$ , since  $V_{sd} = \alpha c_1$ , and  $D_{\text{rxn}} = \kappa c_1/2$ , so that  $\chi D_{\text{rxn}} = \alpha c_1/2$ . Equation (5) is written as

$$w \approx \sum_{i=1}^N \left( \kappa c_1 + \tilde{\omega} \mathbf{u}_i \cdot \kappa \nabla c_1 - \frac{\alpha c_1}{2} \mathbf{u}_i \cdot (\nabla - \beta \mathbf{F}_i^P) \right) \delta(\mathbf{x} - \mathbf{X}_i). \quad (6)$$

In Fig. 12, we plot the relative importance of the second and third terms in eq. (6) compared to the first term as a function of time. We see that the second and third terms are subdominant, and their contribution diminishes further if one considers an average over time.

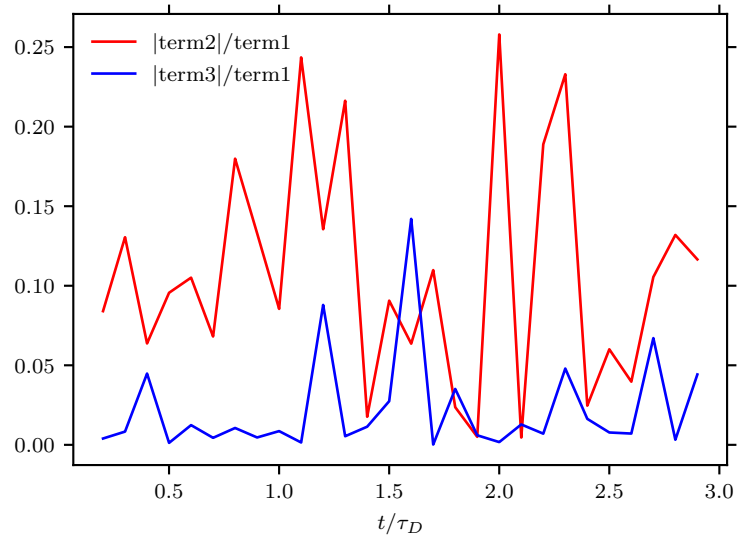


FIG. 12: Relative importance of the second and third terms compared to the first in eq. (6).

---

[1] P. Gaspard and R. Kapral, Active matter, microreversibility, and thermodynamics, Research (2020).